SCIENCE CHINA Materials ARTICLES

mater.scichina.com link.springer.com

Published online 20 January 2021 | https://doi.org/10.1007/s40843-020-1582-3
Sci China Mater 2021, 64(7): 1671–1678

Highly dispersed $L1_0$-PtZn intermetallic catalyst for efficient oxygen reduction

Tuo Zhao[1,2], Ergui Luo[1,2], Yang Li[1,2], Xian Wang[1,2], Changpeng Liu[1,2], Wei Xing[1,2] and Junjie Ge[1,2*]

ABSTRACT **Highly active and durable electrocatalysts with minimal Pt usage are desired for commercial fuel cell applications. Herein, we present a highly dispersed $L1_0$-PtZn intermetallic catalyst for the oxygen reduction reaction (ORR), in which a Zn-rich metal–organic framework (MOF) is used as an *in situ* generated support to confine the growth of PtZn particles. Despite requiring high-temperature treatment, the intermetallic $L1_0$-PtZn particles exhibit a small mean size of 3.95 nm, which confers the catalysts with high electrochemical active surface area (81.9 m^2 g_{Pt}^{-1}) and atomic utilization. The Pt electron structure and binding strength between Pt and oxygen intermediates are optimized through ligand effect and compressive strain. These advantages result in ORR mass activity and specific activity of 0.926 A mg_{Pt}^{-1} and 1.13 mA cm^{-2}, respectively, which are 5.4 and 4.0 times those of commercial Pt/C. The stable $L1_0$ structure provides the catalysts with superb durability; only a halfwave potential loss of 11 mV is observed after 30,000 cycles of accelerated stress tests, through which the structure evolves into a more stable PtZn–Pt core–shell structure. Therefore, the development of a Zn-based MOF as a catalyst support is demonstrated, providing a synergy strategy to prepare highly dispersed intermetallic alloys with high activity and durability.**

Keywords: $L1_0$-PtZn intermetallic catalyst, Zn vapor protect, confinement effect, morphological evolution, ORR

INTRODUCTION

Proton exchange membrane fuel cells are attractive next-generation power sources owing to their advantages including high power density, high conversion efficiency and low pollution [1]. Although Pt has been extensively investigated as the most active monometallic element for the oxygen reduction reaction (ORR) in the past years, high Pt loading is required as a result of the sluggish ORR kinetics at the cathode, which restricts the commercialization of fuel cells [2–4]. To address these issues, intense efforts have been devoted to increase the Pt mass activity and specific activity by optimizing the catalyst particle composition, size, structure, and interaction between carrier and particles [5,6].

Introducing secondary transition metals is effective for enhancing the activity of Pt through ligand effect and compressive strain [7–12]. Thus, by selecting appropriate transition metal elements, the d-band center of Pt could be effectively downshifted, thereby weakening the overly strong binding to oxygen species [13,14]. Although first-row transition metals can most effectively boost the catalytic performance, they are unstable under electrochemical conditions due to their much lower standard oxidation potential. To overcome such problem, the synthesis of Pt-based intermetallic alloys as catalysts has emerged as an ideal strategy [15–17], since the ordered Pt structure not only ensures a strong lattice strain but also stabilizes the second metal as a result of the reinforced bonding between Pt and the latter [18–21]. In this regard, Zn is a promising secondary metal for the formation of Pt–Zn intermetallic structures. The smaller atomic radius and lower electronegativity of Zn confer PtZn alloys with much superior activity to that of pure Pt due to compressive strain and a decreased Pt 5d-band center [22]. Moreover, PtZn alloys have lower formation energy than PtCo and PtNi, which is ascribable to the stronger Pt–Zn bonding energy, thus improving the structural stability during fuel cell operation [23,24].

However, achieving ordered intermetallic catalysts is not a trivial task, since high-temperature treatment is typically required, which inevitably leads to severe aggregation and sintering. Hence, the development of an effective strategy to fabricate PtZn intermetallic alloys

[1] State Key Laboratory of Electroanalytical Chemistry, Jilin Province Key Laboratory of Low Carbon Chemical Power, Changchun Institute of Applied Chemistry, Chinese Academy of Sciences, Changchun 130022, China
[2] School of Applied Chemistry and Engineering, University of Science and Technology of China, Hefei 230026, China
* Corresponding author (email: gejj@ciac.ac.cn)

without sacrificing the mass activity is highly desirable. Typically, aggregation during high-temperature annealing can be prevented by using oxides such as MgO and SiO_2 to form a protective shell on the catalyst particles [25,26]. However, such strategy requires additional post-treatment to remove the protective layer, which complicates the process and hinders upscale synthesis.

Herein, we report the synthesis of a highly efficient $L1_0$-PtZn intermetallic ORR catalyst, in which a Zn-based metal–organic framework (MOF) is responsible for the formation of the ordered structure. Specifically, Zn, as a metal node in the MOF precursor, spontaneously incorporates into the Pt entity and forms a stable $L1_0$-PtZn intermetallic structure *via* high-temperature pyrolysis. Moreover, the excessive Zn atoms are volatilized at high temperature during the synthesis process, thus preventing the aggregation of PtZn particles. This results in ordered $L1_0$-PtZn nanoparticles that are stable toward pyrolysis and possess a small mean size of 3.95 nm and high electrochemical active surface area (81.9 m^2 g_{Pt}^{-1}). This $L1_0$-PtZn catalyst shows better ORR activity (0.926 A mg_{Pt}^{-1} of mass activity and 1.13 mA cm^{-2} of specific activity) and durability (11 mV of halfwave potential ($E_{½}$) loss after 30,000 cycles) than commercial 20 wt.% Pt/C owing to the ligand effect and compressive strain. The ORR performance of our catalyst is among the best of recently reported intermetallic compounds (Table S1). Morphological evolution of a Pt shell and a residual $L1_0$-PtZn intermetallic core are observed after accelerated durability tests (ADTs). This study demonstrates a synergy strategy to prepare atomically dispersed $L1_0$-PtZn intermetallic alloys with high activity and durability.

MATERIALS AND METHODS

Materials

Zinc acetate (99.0%, Aladdin), ellagic acid (96.0%, Aladdin) and 1-methyl-2-pyrrolidinone (98.0 %, Aladdin) were used as received without further purification.

Methods

In a typical synthesis of MOF, 0.316 g of ellagic acid and 0.46 g of zinc acetate were dissolved with 40 mL of 1-methyl-2-pyrrolidinone in a beaker under stirring. After two days of reaction, the precipitate was centrifuged by centrifugation with 1-methyl-2-pyrrolidinone and ethanol, and then dried at 55°C in a drying baker.

For the synthesis of pyrolyzed carbon (C_{MOF}), the as-prepared MOF was heat-treated at 950°C for 2 h under Ar/H_2 with a gas flow ratio of 90/10.

For the synthesis of Pt/C_{MOF}, 75 mg of C_{MOF} and 2.4 mg of Pt (1 mg_{Pt} mL^{-1}, chloroplatinic acid solution, homemade) were stirred for 2 h in 40 mL ethanol. After centrifuging and drying, the precursor was heat-treated at 950°C for 2 h under Ar/H_2 with a gas flow ratio of 90/10, yielding around 50 mg of Pt/C_{MOF}.

For the synthesis of $L1_0$-PtZn/C_{MOF}, 0.53 g of MOF and 4.4 mg of Pt (1 mg_{Pt} mL^{-1}, chloroplatinic acid solution, self-configured) were stirred for 2 h in 40 mL ethanol. After centrifuging and drying, the precursor was heat-treated at 950°C for 2 h under Ar/H_2 with a gas flow ratio of 90/10. Around 100 mg of PtZn/C_{MOF} was obtained.

Characterizations

Scanning electron microscopy (SEM) measurements were performed with an XL 30 ESEMFEG field emission scanning electron microscope. Transmittance electron microscopy (TEM) and elemental mapping analysis were conducted on a Philips TECNAI G2 electron microscope operated at 200 kV. Powder XRD measurements were performed on a PW1700 diffractometer (Philips Co.) with a Cu Kα (λ = 0.15405 nm) radiation source operated at 40 kV and 30 mA. The textural and morphological features of precursors and catalysts were determined by nitrogen physisorption at 77 K with a Micromeritics ASAP 2020. X-ray photoelectron spectroscopy (XPS) measurements were performed using a Kratos XSAM-800 spectrometer with an Mg Kα radiation source.

Electrochemical measurements

The electrochemical measurements were conducted using a 750E Bipotentiostat (CH Instruments). The catalyst ink was prepared by dispersing 5 mg of catalyst ultrasonically in a mixture containing 50 μL of Nafion (5 wt%) solution, 550 μL of isopropanol, and 400 μL of deionized water. The catalyst film-coated electrode was obtained by dispersing the catalyst ink on a glassy carbon rotating disk electrode (RDE) or a rotating ring-disk electrode (RRDE) followed by drying in air. The catalyst loading on the electrode was 20 μg_{Pt} cm^{-2} for Pt/C and 12 μg_{Pt} cm^{-2} for PtZn/C_{MOF}. A conventional three-electrode cell comprising a reversible hydrogen electrode (RHE) as the reference electrode, a graphite rod as the counter electrode, and the catalyst film-coated RDE or RRDE as the working electrode was employed. A 0.1 mol L^{-1} $HClO_4$ solution was used as the electrolyte for the ORR test. A 90% *IR* correction was performed during the ORR test. RRDE measurements were conducted by linear sweep voltammetry (LSV) from 0.05 to 1.03 V with a scan rate of

10 mV s^{-1} at 1600 rpm. The H_2O_2 collection coefficient at the ring in the RRDE experiments was 0.37. The following equations were used to calculate the apparent number of electrons transferred during ORR (n) and the percentage of H_2O_2 released during ORR:

$$n = \frac{4I_D}{I_D + (I_R/N)}, \quad (1)$$

$$H_2O_2\% = 100\frac{2I_R/N}{I_D + (I_R/N)}, \quad (2)$$

where I_D is the Faradaic current at the disk, I_R is the Faradaic current at the ring, and N is the H_2O_2 collection coefficient at the ring.

The ORR results were presented after subtracting the currents measured in N_2-saturated 0.1 mol L^{-1} $HClO_4$ electrolyte to remove capacitive currents. ADTs were performed at room temperature in O_2-saturated 0.1 mol L^{-1} $HClO_4$ solution by applying cyclic potential sweeps between 0.6 and 1.0 V *versus* RHE at a sweep rate of 200 mV s^{-1} for 30,000 cycles, and the initial and final LSV curves were collected. We collected electrolyte samples at 5000, 10,000, 20,000, and 30,000 cycles to determine the loss of Pt and Zn by inductively coupled plasma (ICP).

RESULTS AND DISCUSSION

First, we synthesized a Zn-based MOF using ellagic acid and $Zn(OAc)_2$ as precursors (Fig. 1a) [27]. The MOF structure consisted of staggered nanosheets and an overall spherical morphology (Fig. 1b and Figs S1, S2), which was well retained after pyrolysis (Fig. S3). The carbon obtained after pyrolysis (denoted as C_{MOF} hereafter) exhibited interlaced nanosheets (Fig. S4) and much higher specific surface area than the MOF precursor (882 m^2 g^{-1} for C_{MOF} and 27.9 m^2 g^{-1} for MOF). Specifically, the N_2 adsorption–desorption isotherm of C_{MOF} exhibits a type

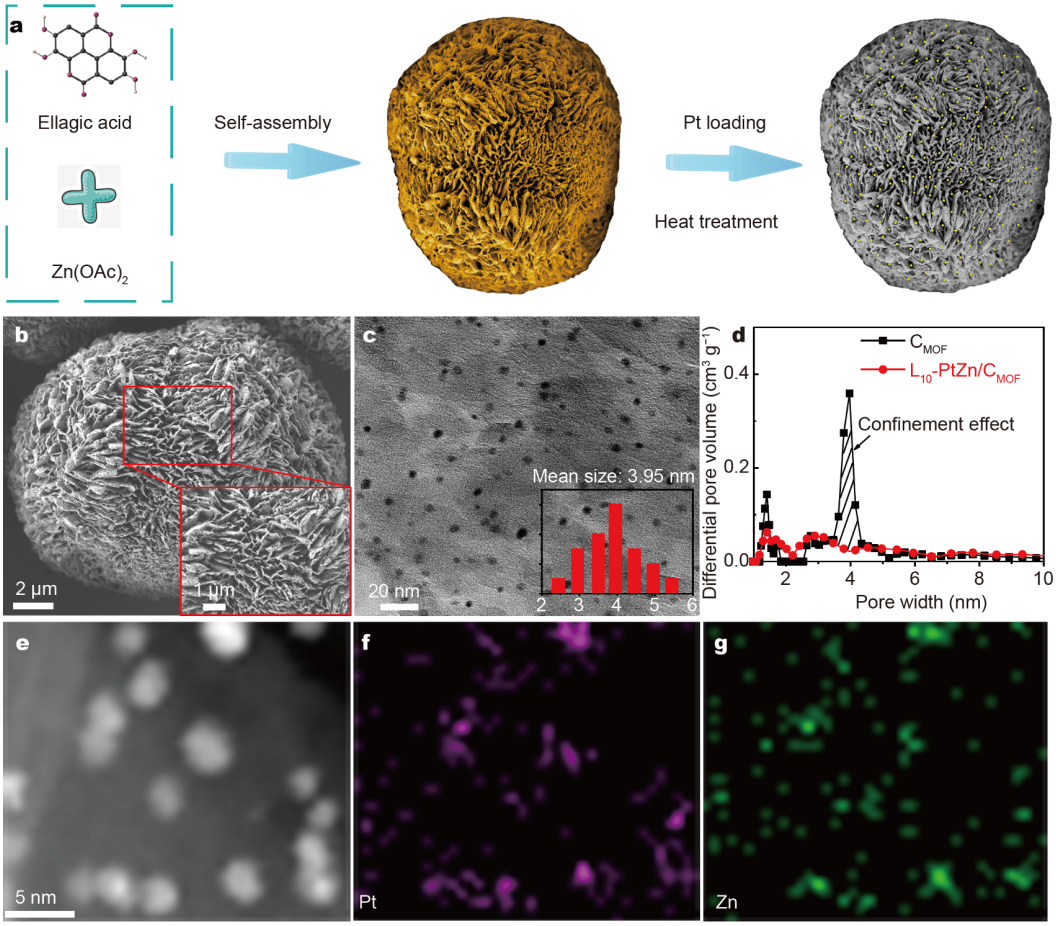

Figure 1 Synthetic scheme, structure with interlaced nanosheets, and morphology of $L1_0$-PtZn/C_{MOF}. (a) Synthetic procedures for $L1_0$-PtZn/C_{MOF}. (b) SEM images of MOF. (c) TEM image and particle-size distribution of $L1_0$-PtZn/C_{MOF}. (d) Pore-size distribution of $L1_0$-PtZn/C_{MOF} and C_{MOF}. (e) HAADF-STEM image of $L1_0$-PtZn/C_{MOF}. (f, g) EDS elemental mappings of Pt and Zn, respectively.

IV hysteresis loop at medium relative pressure (Fig. S5), revealing its mesoporous nature. The density functional theory (DFT) analysis shows a major peak located at 2 nm for MOF and 4 nm for C_{MOF} (Fig. 1d and Fig. S5), further verifying the mesoporous nature of the carbon material. This mesoporous carbon structure, which is beneficial for anchoring the metal particles and for mass transfer during fuel cell operation, renders C_{MOF} an ideal support.

The synthesis of the C_{MOF}-supported $L1_0$-PtZn catalyst was performed by simply introducing the Pt precursor into the MOF structure before pyrolysis. In this system, a host–guest mechanism can be considered responsible for the high dispersion of the final Pt catalyst. As shown in Fig. 1c, PtZn particles with a mean particle size of 3.95 nm and high dispersion were achieved after pyrolysis at 950°C for 2 h. Interestingly, the particle size of PtZn is in good correlation with the pore size of C_{MOF} (both around 4 nm), which suggests that the hierarchical pore exerts a confinement effect limiting the particle growth. This hypothesis was supported by DFT analysis, which showed that the introduction of Pt led to a restricted pore width of 4 nm (Fig. 1d). Meanwhile, the *in situ* generation of Zn vapor was also crucial to prevent particle agglomeration. This was demonstrated by synthesizing a control Pt/C_{MOF} sample, in which C_{MOF} was used to load Pt followed by a second pyrolysis process. In the control sample, the nanoparticle aggregation was observed (Fig. S6). We then investigated the catalyst composition by ICP optical emission spectrometry (ICP-OES). Interestingly, the catalyst exhibited mass fractions of Pt and Zn of 4.4% and 1.4%, respectively, demonstrating a Pt/Zn atom ratio of 1:1. However, in the absence of Pt, Zn was vaporized during the pyrolysis, leaving carbon as the sole product (Table S2). These results indicate that Pt has a strong tendency to bind with Zn, thereby leading to the spontaneous formation of the PtZn bimetal structure. Taken together, these results demonstrate that the combination of the confinement effect of the MOF, according to which mesopores of around 4 nm are filled with PtZn nanoparticles, and the Zn vapor protecting strategy, which restrains the particle growth, prevents particle aggregation at high temperature.

High-annular dark-field scanning transmission electron microscopy (HAADF-STEM) and scanning transmission electron microscopy-energy dispersive spectrometry (STEM-EDS) elemental mapping of $L1_0$-PtZn/C_{MOF} (Fig. 1e–g) reveal that the distribution of Zn resembles that of Pt, thus confirming the alloy feature. The atomic ratio (Fig. S7) of Pt/Zn was determined to be 1:1 by EDS, which is consistent with the ICP result. The powder X-ray diffraction (XRD) pattern of $L1_0$-PtZn/C_{MOF} (Fig. 2c) agrees well with the intermetallic $L1_0$-PtZn PDF card (PDF#06-0604) without any impurity peak, demonstrating the formation of an ordered $L1_0$-PtZn intermetallic structure. The super lattice peaks observed at 31.3° and 25.3° can be assigned to the (110) and (001) planes of $L1_0$-PtZn, and an intensity ratio of 0.30 for (110)/(111), which is close to that of the bulk $L1_0$-PtZn, and further verifies the ordered structure [28]. The high-resolution TEM (HRTEM) images depicted in Fig. 2a, b reveal the presence of lattice fringes of 0.221 and 0.351 nm, corresponding to the (111) and (001) facets of the PtZn intermetallic structure. An evident lattice shrinkage in comparison to Pt/C (0.226 nm for (111)) was noticed, corresponding to 2.2% compressive strain. The intensified d-orbital overlapping caused the d-band center to shift downward, resulting in weakened adsorption properties of the reaction intermediates, which is beneficial for the enhancement of the binding strength [29,30]. We then investigated the electronic property of $L1_0$-PtZn/C_{MOF} and Pt/C by XPS. A negative shift was observed in the Pt core levels (71.7 eV for Pt 4f) compared with those of Pt/C (71.9 eV for Pt 4f) (Fig. 2d). Furthermore, the Zn core levels (1022.0 eV for Zn 2p) (Fig. S8) underwent a positive shift compared with pure Zn (1021.5 eV for Zn 2p). Since the XRD results reveal that Zn and Pt are bonded strongly in the intermetallic alloy, these electronic changes are most likely caused by electron donation from Zn to Pt. This electron transfer can downshift the Pt d-band center, thus optimizing the binding affinity between Pt and oxygen intermediates [3,31–33].

We then conducted electrochemical tests to evaluate the ORR performance of the catalyst. First, the electrochemical active surface area was evaluated through CO stripping (Fig. 3a) and hydrogen underpotential deposition (Fig. S9, the hydrogen area was covered). The $L1_0$-PtZn/C_{MOF} and Pt/C catalyst exhibited surface areas of 81.9 and 60.1 $m^2\ g_{Pt}^{-1}$, respectively, with the former higher due to its smaller particle size (3.95 nm). Second, the $E_{½}$ (Fig. 3b) of $L1_0$-PtZn/C_{MOF} (0.922 V) was much higher than that of commercial Pt/C (0.880 V), Pt/C_{MOF} (0.881 V), and C_{MOF}, according to LSV recorded in an O_2-saturated 0.1 mol L^{-1} $HClO_4$ solution. The LSV analysis also revealed that the Tafel slope of $L1_0$-PtZn/C_{MOF} (67 mV dec^{-1}) was smaller than that of Pt/C (75 mV dec^{-1}), indicating the enhanced ORR kinetics for the former (Fig. 3c). The electron transfer number (3.98) calculated from the RRDE (Fig. S10) is consistent with a complete four-electron pathway from O_2 to H_2O with scarce generation of H_2O_2. Furthermore, $L1_0$-PtZn/C_{MOF}

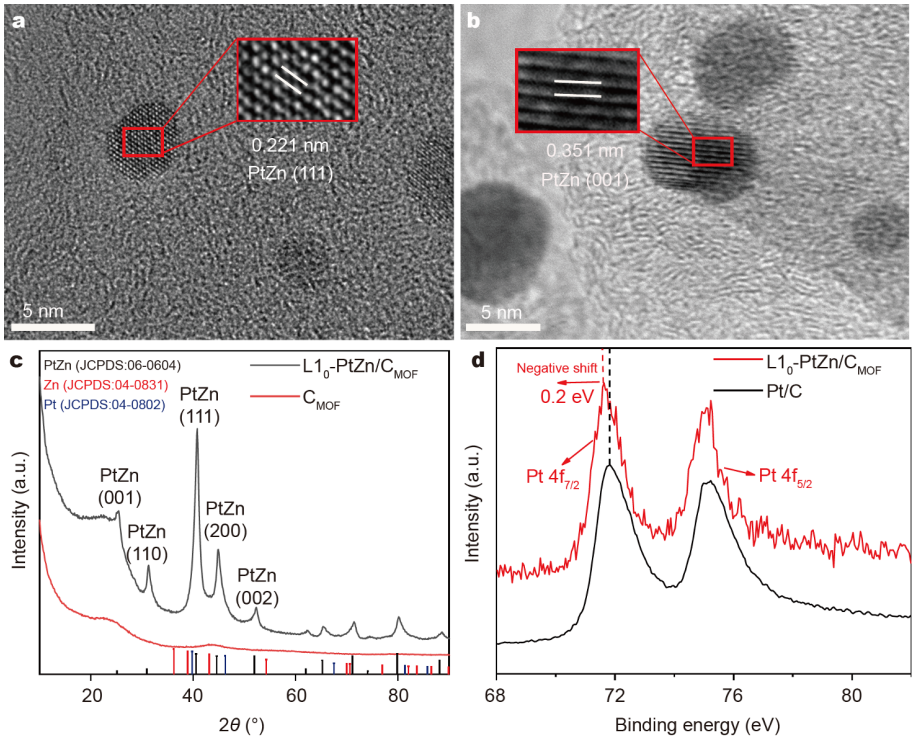

Figure 2 Structure and composition of $L1_0$-PtZn/C_{MOF}. (a, b) HRTEM images and lattice fringes of $L1_0$-PtZn/C_{MOF}. (c) XRD patterns of $L1_0$-PtZn/C_{MOF} and C_{MOF}. (d) XPS spectra of $L1_0$-PtZn/C_{MOF} and Pt/C.

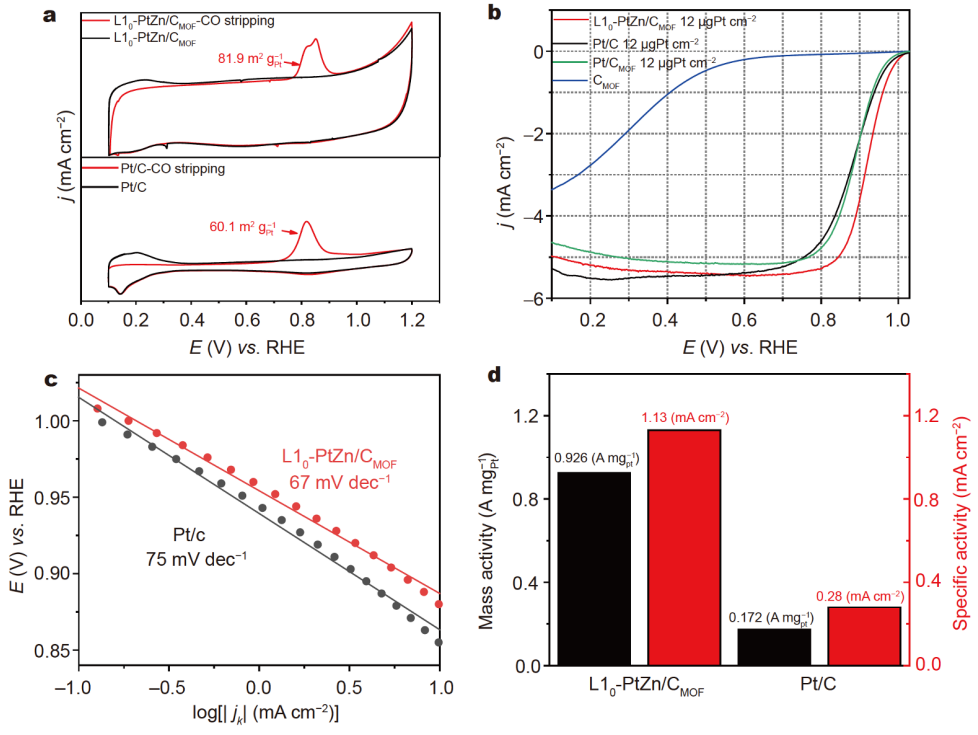

Figure 3 Electrochemical performance of $L1_0$-PtZn/C_{MOF} and Pt/C. (a) cyclic voltammetry (CV) and CO stripping curves of $L1_0$-PtZn/C_{MOF} and Pt/C. (b) LSV curves of different samples. (c) Tafel plots of $L1_0$-PtZn/C_{MOF} and Pt/C. (d) Mass activity and specific activity of $L1_0$-PtZn/C_{MOF} and Pt/C.

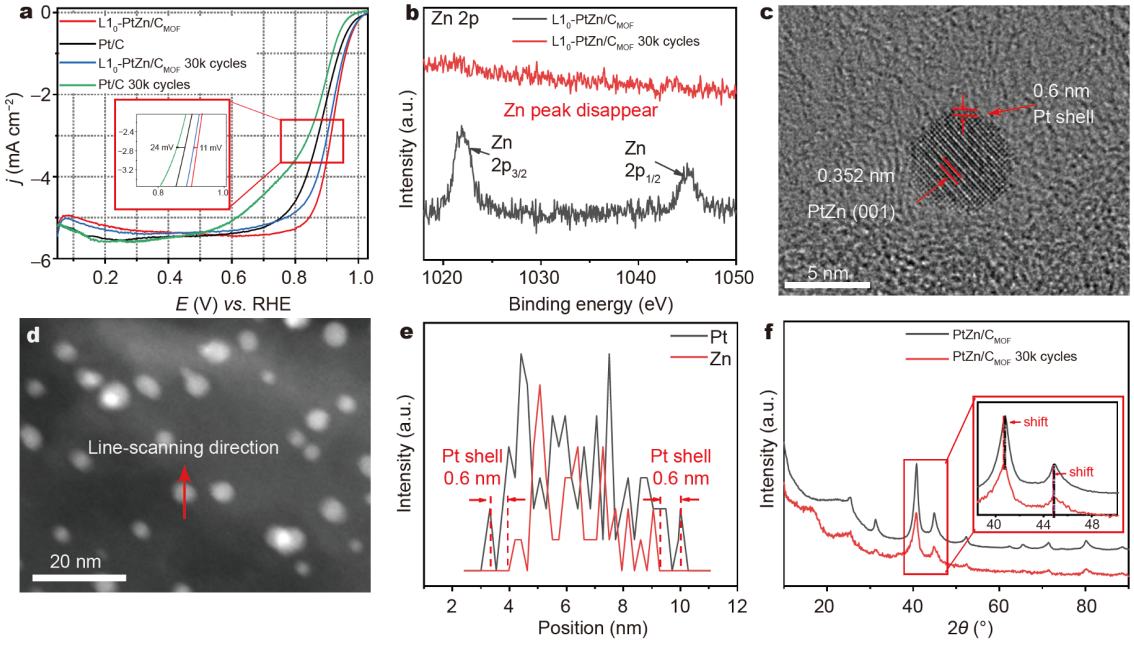

Figure 4 Durability performance and morphological evolutions. (a) LSV curves of L1$_0$-PtZn/C$_{MOF}$ and Pt/C after ADTs. (b) Zn peak changes of the XPS spectra. (c) Lattice fringes and Pt shell after ADTs. (d, e) HAADF line profiles showing the Pt shell. (f) XRD peak changes of L1$_0$-PtZn/C$_{MOF}$.

exhibited mass activity of 0.926 A mg_{Pt}^{-1} and specific activity of 1.13 mA cm^{-2} at 0.9 V *versus* an RHE (Fig. 3d), which were respectively 5.4 and 4.0 times those of the Pt/C reference sample (0.172 A mg_{Pt}^{-1} and 0.28 mA cm^{-2}). According to the electrochemical tests, it can be concluded that the incorporation of Zn and the formation of the intermetallic alloy between Pt and Zn are beneficial for improving the ORR performance.

In addition to activity, durability is an important evaluation criterion for catalyst applicability; therefore, L1$_0$-PtZn/C$_{MOF}$ was subjected to ADTs for 30,000 cycles between 0.6 and 1.0 V in an O_2-saturated 0.1 mol L^{-1} $HClO_4$ solution. Its high durability was evidenced by an $E_{½}$ loss of 11 mV (Fig. 4a), which is much smaller than that of Pt/C (24 mV $E_{½}$ loss), demonstrating the more robust nature of L1$_0$-PtZn/C$_{MOF}$ compared with Pt/C during the test. To explore the reason for this high durability, the morphology, composition, electronic state, and structure of L1$_0$-PtZn/C$_{MOF}$ were studied after ADTs. The particle size did not change significantly (Fig. S11), and Zn and Pt remained together (Fig. S12). This good morphology stability toward migration and agglomeration is beneficial for maintaining high ORR performance [34,35]. With regard to composition changes, since the second metals are usually difficult to preserve due to their more active chemical properties, we investigated the electrolyte composition changes of Pt and Zn at different cycles during ADTs. The ICP results (Table S3) showed that Pt was well retained during the whole ADTs, whereas 1/3 Zn was lost before 5000 cycles. The rest of Zn remained until 30,000 cycles, indicating that L1$_0$-PtZn/C$_{MOF}$ was stable after 5000 cycles. Interesting changes were observed when evaluating the electronic state. Thus, the Zn peak disappeared in the XPS spectra (Fig. 4b), suggesting that the Zn on the nanoparticle surface dissolved, and a Pt shell was eventually formed. This morphological evolution was further demonstrated by HRTEM (Fig. 4c, Fig. S13); the lattice fringes inside the nanoparticles no longer extended to the surface, and a Pt shell was observed on the surface [36]. The thickness of this Pt shell was about 0.6 nm (Fig. 4c–e), which corresponds to 3–4 atomic Pt layers. Structurally, the XRD patterns depicted in Fig. 4f show that the peaks shifted slightly to lower angles because the smaller atomic radius of Zn was reduced one third after ADTs, being 0.353 nm for the (001) and 0.288 nm for the (110) interplanar fringes (Fig. S13), further demonstrating that the L1$_0$-PtZn structure changed throughout the ADTs. Considering the above comprehensive analysis, we conclude that a core–shell structure with a PtZn intermetallic core and a Pt shell eventually formed after ADTs.

This core–shell structure contributes to maintain ORR activity and stability, protecting the PtZn particles against further Zn leaching from the inner region [32,37–41].

CONCLUSIONS

Benefiting from the confinement effect of the MOF and a Zn vapor protective feature, we successfully prepared an $L1_0$-PtZn intermetallic ORR catalyst with small particle size (3.95 nm) using a Zn-rich MOF as support for the particle growth. The $L1_0$-PtZn catalyst shows high mass activity (0.926 A mg_{Pt}^{-1}) and specific activity (1.13 mA cm^{-2}), which are 5.4 and 4.0 times those of commercial Pt/C. In ADTs, the catalyst shows robust stability with an $E_{½}$ decay of 11 mV after 30,000 cycles, and the intermetallic particles undergo morphological evolution to an intermetallic core with a Pt shell. XRD, TEM, and other experimental results reveal that the admirable ORR performance can be ascribed to the alloying affect and compressive strain around the $L1_0$-PtZn intermetallic alloy. Therefore, a synergy strategy to prepare highly dispersed intermetallic alloys is demonstrated, which involves a clear morphology evolution that prevents particle agglomeration at high temperature. This study can contribute to the rational design of electrocatalysts for practical applications.

Received 27 September 2020; accepted 27 November 2020; published online 20 January 2021

1 Wang YJ, Wilkinson DP, Zhang J. Noncarbon support materials for polymer electrolyte membrane fuel cell electrocatalysts. Chem Rev, 2011, 111: 7625–7651
2 Gasteiger HA, Marković NM. Just a dream—or future reality? Science, 2009, 324: 48–49
3 Greeley J, Stephens IEL, Bondarenko AS, *et al.* Alloys of platinum and early transition metals as oxygen reduction electrocatalysts. Nat Chem, 2009, 1: 552–556
4 Kulkarni A, Siahrostami S, Patel A, *et al.* Understanding catalytic activity trends in the oxygen reduction reaction. Chem Rev, 2018, 118: 2302–2312
5 Zhou W, Wu J, Yang H. Highly uniform platinum icosahedra made by hot injection-assisted grails method. Nano Lett, 2013, 13: 2870–2874
6 Chen C, Kang Y, Huo Z, *et al.* Highly crystalline multimetallic nanoframes with three-dimensional electrocatalytic surfaces. Science, 2014, 343: 1339–1343
7 Strasser P, Koh S, Anniyev T, *et al.* Lattice-strain control of the activity in dealloyed core–shell fuel cell catalysts. Nat Chem, 2010, 2: 454–460
8 Bu L, Zhang N, Guo S, *et al.* Biaxially strained PtPb/Pt core/shell nanoplate boosts oxygen reduction catalysis. Science, 2016, 354: 1410–1414
9 Shao M, Chang Q, Dodelet JP, *et al.* Recent advances in electrocatalysts for oxygen reduction reaction. Chem Rev, 2016, 116: 3594–3657
10 Stamenkovic VR, Strmcnik D, Lopes PP, *et al.* Energy and fuels from electrochemical interfaces. Nat Mater, 2016, 16: 57–69
11 Stephens IEL, Rossmeisl J, Chorkendorff I. Toward sustainable fuel cells. Science, 2016, 354: 1378–1379
12 Luo M, Guo S. Strain-controlled electrocatalysis on multimetallic nanomaterials. Nat Rev Mater, 2017, 2: 17059
13 Stamenkovic VR, Mun BS, Arenz M, *et al.* Trends in electrocatalysis on extended and nanoscale Pt-bimetallic alloy surfaces. Nat Mater, 2007, 6: 241–247
14 Hwang SJ, Kim SK, Lee JG, *et al.* Role of electronic perturbation in stability and activity of pt-based alloy nanocatalysts for oxygen reduction. J Am Chem Soc, 2012, 134: 19508–19511
15 Ji X, Lee KT, Holden R, *et al.* Nanocrystalline intermetallics on mesoporous carbon for direct formic acid fuel cell anodes. Nat Chem, 2010, 2: 286–293
16 Iihama S, Furukawa S, Komatsu T. Efficient catalytic system for chemoselective hydrogenation of halonitrobenzene to haloaniline using PtZn intermetallic compound. ACS Catal, 2015, 6: 742–746
17 Wang W, Lei B, Guo S. Engineering multimetallic nanocrystals for highly efficient oxygen reduction catalysts. Adv Energy Mater, 2016, 6: 1600236
18 Furukawa S, Komatsu T. Intermetallic compounds: Promising inorganic materials for well-structured and electronically modified reaction environments for efficient catalysis. ACS Catal, 2017, 7: 735–765
19 Luo M, Sun Y, Wang L, *et al.* Tuning multimetallic ordered intermetallic nanocrystals for efficient energy electrocatalysis. Adv Energy Mater, 2017, 7: 1602073
20 Yang Y, Xiao W, Feng X, *et al.* Golden palladium zinc ordered intermetallics as oxygen reduction electrocatalysts. ACS Nano, 2019, 13: 5968–5974
21 Xiao W, Lei W, Gong M, *et al.* Recent advances of structurally ordered intermetallic nanoparticles for electrocatalysis. ACS Catal, 2018, 8: 3237–3256
22 Sode A, Li W, Yang Y, *et al.* Electrochemical formation of a Pt/Zn alloy and its use as a catalyst for oxygen reduction reaction in fuel cells. J Phys Chem B, 2006, 110: 8715–8722
23 Yan Y, Du JS, Gilroy KD, *et al.* Intermetallic nanocrystals: Syntheses and catalytic applications. Adv Mater, 2017, 29: 1605997
24 Liang J, Ma F, Hwang S, *et al.* Atomic arrangement engineering of metallic nanocrystals for energy-conversion electrocatalysis. Joule, 2019, 3: 956–991
25 Li Q, Wu L, Wu G, *et al.* New approach to fully ordered fct-FePt nanoparticles for much enhanced electrocatalysis in acid. Nano Lett, 2015, 15: 2468–2473
26 Zhao EW, Maligal-Ganesh R, Xiao C, *et al.* Silica-encapsulated Pt-Sn intermetallic nanoparticles: A robust catalytic platform for parahydrogen-induced polarization of gases and liquids. Angew Chem Int Ed, 2017, 56: 3925–3929
27 Yang SJ, Antonietti M, Fechler N. Self-assembly of metal phenolic mesocrystals and morphosynthetic transformation toward hierarchically porous carbons. J Am Chem Soc, 2015, 137: 8269–8273
28 Cui Z, Chen H, Zhao M, *et al.* High-performance Pd_3Pb intermetallic catalyst for electrochemical oxygen reduction. Nano Lett, 2016, 16: 2560–2566
29 Zhang S, Zhang X, Jiang G, *et al.* Tuning nanoparticle structure and surface strain for catalysis optimization. J Am Chem Soc, 2014, 136: 7734–7739
30 Wang H, Xu S, Tsai C, *et al.* Direct and continuous strain control of catalysts with tunable battery electrode materials. Science, 2016,

354: 1031–1036
31 Li J, Xi Z, Pan YT, *et al.* Fe stabilization by intermetallic $L1_0$-FePt and Pt catalysis enhancement in $L1_0$-FePt/Pt nanoparticles for efficient oxygen reduction reaction in fuel cells. J Am Chem Soc, 2018, 140: 2926–2932
32 Oezaslan M, Hasché F, Strasser P. Pt-based core–shell catalyst architectures for oxygen fuel cell electrodes. J Phys Chem Lett, 2013, 4: 3273–3291
33 Jung N, Chung DY, Ryu J, *et al.* Pt-based nanoarchitecture and catalyst design for fuel cell applications. Nano Today, 2014, 9: 433–456
34 Ho VTT, Pan CJ, Rick J, *et al.* Nanostructured $Ti_{0.7}Mo_{0.3}O_2$ support enhances electron transfer to Pt: High-performance catalyst for oxygen reduction reaction. J Am Chem Soc, 2011, 133: 11716–11724
35 Zhang B, Fu G, Li Y, *et al.* General strategy for synthesis of ordered Pt_3M intermetallics with ultrasmall particle size. Angew Chem Int Ed, 2020, 59: 7857–7863
36 Tian X, Zhao X, Su YQ, *et al.* Engineering bunched Pt-Ni alloy nanocages for efficient oxygen reduction in practical fuel cells. Science, 2019, 366: 850–856
37 Wang X, Vara M, Luo M, *et al.* Pd@Pt core–shell concave decahedra: a class of catalysts for the oxygen reduction reaction with enhanced activity and durability. J Am Chem Soc, 2015, 137: 15036–15042
38 Zhao X, Chen S, Fang Z, *et al.* Octahedral $Pd@Pt_{1.8}Ni$ core–shell nanocrystals with ultrathin PtNi alloy shells as active catalysts for oxygen reduction reaction. J Am Chem Soc, 2015, 137: 2804–2807
39 Mazumder V, Chi M, More KL, *et al.* Core/shell Pd/FePt nanoparticles as an active and durable catalyst for the oxygen reduction reaction. J Am Chem Soc, 2010, 132: 7848–7849
40 Wang D, Xin HL, Yu Y, *et al.* Pt-decorated PdCo@Pd/C core–shell nanoparticles with enhanced stability and electrocatalytic activity for the oxygen reduction reaction. J Am Chem Soc, 2010, 132: 17664–17666
41 Guo S, Zhang S, Su D, *et al.* Seed-mediated synthesis of core/shell FePtM/FePt (M = Pd, Au) nanowires and their electrocatalysis for oxygen reduction reaction. J Am Chem Soc, 2013, 135: 13879–13884

Acknowledgements This work was supported by the National Science and Technology Major Project (2017YFB0102900), the National Natural Science Foundation of China (21633008, 21673221 and U1601211), and Jilin Province Science and Technology Development Program (20200201001JC, 20190201270JC and 20180101030JC).

Author contributions Ge J supervised the study. Zhao T designed the experiments, performed most of the experiments and characterizations. Luo E, Li Y and Wang X participated in the analyses of the results. Zhao T wrote the manuscript, and Ge J, Liu C and Xing W revised it. All the authors contributed to the general discussion.

Conflict of interest The authors declare that they have no conflict of interest.

Supplementary information Supporting data are available in the online version of the paper.

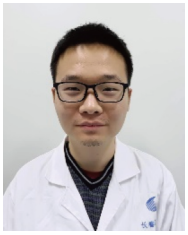

Tuo Zhao is a PhD candidate at the State Key Laboratory of Electroanalytical Chemistry, Changchun Institute of Applied Chemistry (CIAC). He received his BSc degree in materials science and engineering from Hainan University in 2016. His current research interest is the development of efficient ORR catalysts in proton exchange membrane fuel cells.

Junjie Ge is a professor of chemistry at CIAC, Chinese Academy of Sciences (CAS). She received her PhD in physical chemistry from CIAC in 2010 and completed postdoctoral training at the University of South Carolina (2010-2012) and University of Hawaii (2012-2015). She joined CIAC in 2015 as a professor, where she was recruited in the Hundred Talents Program in CAS (2015). Her current research interests focus on hydrogen energy and fuel cells, basic electrochemistry, and electrocatalysis, mainly concentrating in proton exchange membrane-based energy conversion systems.

高分散$L1_0$-PtZn金属间化合物高效催化氧还原

赵拓[1,2], 罗二桂[1,2], 李阳[1,2], 王显[1,2], 刘长鹏[1,2], 邢巍[1,2], 葛君杰[1,2*]

摘要 燃料电池商业化的关键在于实现低铂催化剂的高活性和高耐久性. 本文通过使用一种富锌MOF作为原位生长的载体来限制PtZn粒子增长, 成功制备了高分散的$L1_0$-PtZn金属间化合物氧还原反应(ORR)催化剂. 该催化剂经过高温处理后平均粒径仅为3.95 nm, 具有较高的电化学活性表面积(81.9 m^2 g_{Pt}^{-1})和原子利用率. 配体效应和压缩应变优化了铂的电子结构, 从而调节了铂与氧中间体之间的结合强度. 催化剂表现出高的质量活性(0.926 A mg_{Pt}^{-1})和比活性(1.13 mA cm^{-2}), 分别为商业Pt/C催化剂(0.172 A mg_{Pt}^{-1}和0.28 mA cm^{-2})的5.4倍和4.0倍. 由于$L1_0$自身结构更加稳定, 并且PtZn金属纳米粒子在耐久循环中逐步演变为PtZn-Pt核壳结构, 使得该催化剂在30,000圈加速老化测试中表现出优异的稳定性(仅11 mV半波电位($E_{1/2}$)损耗).

